ISSN: 2640-5571

Research Article

Advances in Nanoscience and Nanotechnology

Novel g-C_3N_4/$CdTiO_3$ Heterostructures with Improved Photocatalytic Activity Under Visible Light Irradiation

Pramendra Kumar Pandey[1], Revati Raman Chaubey[2], Arvind Kumar Singh[3], Gyandeshwar K Rao[4] and Bharat Kumar[1*]

[1]*Department of Chemistry, M V College Buxar (Constituent unit of Veer Kunwar Singh University Ara), India*

[2]*Department of Chemistry, Indira Gandhi National Tribal University Amarkantak, India*

[3]*Department of Chemistry, S B College Ara (Constituent unit of Veer Kunwar Singh University Ara), India*

[4]*Department of Chemistry, Kisan College Nalanda (Constituent unit of Patliputra University Patna), India*

***Corresponding Author**
Bharat Kumar, Department of Chemistry, M V College Buxar (Constituent unit of Veer Kunwar Singh University Ara), India.

Submitted: 2026, Feb 27; **Accepted:** 2026, Mar 23; **Published:** 2026, Mar 30

Citation: Pandey, P. K., Chaubey, R. R., Singh, A. K., Rao, G. K., Kumar, B. (2026). Novel g-C_3N_4/$CdTiO_3$ Heterostructures with Improved Photocatalytic Activity Under Visible Light Irradiation. *Adv Nanoscie Nanotec, 10*(1), 01-13.

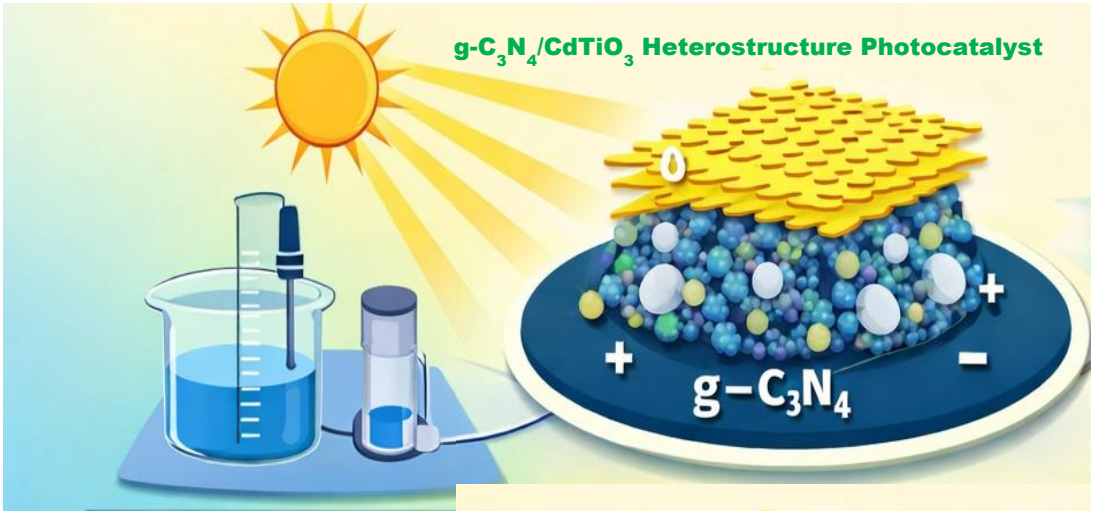

Sunlight-Driven g-C_3N_4/$CdTiO_3$ Heterostructure Enables Efficient Charge Separation for Enhanced Photocatalytic Activity

Highlights

- Visible-light active g-C_3N_4/$CdTiO_3$ heterostructure successfully synthesized
- Efficient S-scheme charge transfer enhances electron–hole separation
- Significantly improved photocatalytic degradation of RhB dye
- Generation of reactive species (•OH and O_2^-) boosts activity
- Excellent stability and reusability for wastewater treatment applications

Abstract

The persistent presence of organic dyes in wastewater poses a serious threat to aquatic ecosystems and human health, necessitating the development of efficient visible-light-responsive photocatalysts. In this study, a g-C_3N_4/$CdTiO_3$ heterostructured photocatalyst was synthesized via sonication and in-situ approaches for the enhanced photocatalytic degradation of Rhodamine B (RhB) under visible-light irradiation. Structural and microscopic analyses revealed the formation of an intimate heterointerface between thin, layered g-C_3N_4 nanosheets and $CdTiO_3$ particles, which facilitates rapid interfacial charge transfer. The composite exhibited broadened visible-light absorption and significantly suppressed electron–hole recombination compared to the individual components. Band alignment analysis suggests that the photocatalytic process proceeds via an S-scheme heterojunction mechanism, retaining highly oxidative holes and strongly reductive electrons responsible for efficient RhB degradation. The optimized g-C_3N_4/$CdTiO_3$ nanocomposite showed markedly enhanced RhB removal efficiency and reaction kinetics relative to pristine g-C_3N_4 and $CdTiO_3$. Furthermore, the catalyst demonstrated excellent stability and repeatability over successive photocatalytic cycles, indicating strong structural integrity and reusability. The improved photocatalytic performance is attributed to synergistic effects arising from effective charge separation, strong interfacial interaction, and preserved redox capability. This work highlights the potential of g-C_3N_4/$CdTiO_3$ S-scheme heterostructures as efficient photocatalysts for dye-contaminated wastewater treatment.

Keywords: In-situ, Titanates, Heterostructures, Photocatalysis

1. Introduction

Rapid industrialization and urbanization have resulted in severe environmental pollution and an increasing global energy crisis. The discharge of organic contaminants such as dyes, pesticides, and pharmaceutical residues into aquatic systems poses serious risks to ecosystems and human health. At the same time, the depletion of fossil fuel resources has driven intensive research toward sustainable and renewable energy technologies. In this context, semiconductor-based photocatalysis has emerged as a promising green technology for solar-driven environmental remediation and energy conversion, owing to its ability to utilize abundant solar energy under mild reaction conditions without generating secondary pollution [1-3].

Conventional photocatalysts such as TiO_2 and ZnO have been extensively studied because of their strong oxidation ability, chemical stability, and low cost. However, their wide band gaps severely limit visible-light absorption, which restricts their practical application since visible light constitutes the major portion of the solar spectrum [4,5]. Therefore, the development of visible-light-active photocatalysts with efficient charge separation remains a significant research challenge.

Graphitic carbon nitride (g-C_3N_4), a metal-free polymeric semiconductor composed of carbon and nitrogen, has attracted considerable attention as a visible-light-responsive photocatalyst due to its moderate band gap (~2.7 eV), suitable band edge positions, high chemical and thermal stability, and facile synthesis from inexpensive nitrogen-rich precursors such as melamine or urea [6-8]. Consequently, g-C_3N_4 has been widely explored for photocatalytic degradation of organic pollutants, hydrogen evolution, and CO_2 reduction [9-11]. Nevertheless, pristine g-C_3N_4 suffers from low surface area, poor electrical conductivity, and rapid recombination of photogenerated charge carriers, which significantly limit its photocatalytic efficiency [12,13].

To overcome these limitations, various strategies have been developed, including heteroatom doping, morphological engineering, surface functionalization, and the construction of semiconductor heterojunctions [14-16]. Among them, heterojunction engineering has proven particularly effective in enhancing photocatalytic performance by promoting interfacial charge transfer, extending light absorption, and suppressing electron–hole recombination [17,18]. In recent years, perovskite-type metal oxides have gained increasing interest in photocatalysis owing to their structural flexibility, tunable electronic properties, and excellent chemical stability [19].

Cadmium titanate ($CdTiO_3$), a perovskite oxide semiconductor, exhibits good crystallinity, suitable band alignment, and favorable charge transport characteristics [20,21]. These properties make $CdTiO_3$ a promising candidate for coupling with visible-light-active semiconductors such as g-C_3N_4. In g-C_3N_4/$CdTiO_3$ heterostructures, g-C_3N_4 can act as the primary visible-light absorber, while $CdTiO_3$ facilitates efficient charge separation and transport, thereby suppressing charge recombination through synergistic interfacial interactions.

Although numerous g-C_3N_4-based heterostructures have been reported for visible-light-driven dye degradation—particularly those coupled with metal oxides and titanates such as TiO_2, $SrTiO_3$,

$NiTiO_3$, and $CoTiO_3$. Studies on g-C_3N_4/$CdTiO_3$ nanocomposites remain notably scarce. To the best of our knowledge, no systematic investigation has been reported on the synthesis, interfacial structure, and photocatalytic dye degradation performance of g-C_3N_4/$CdTiO_3$ composites. This clear research gap provides strong motivation for exploring g-C_3N_4/$CdTiO_3$ heterostructures as a new class of visible-light-responsive photocatalysts. In this work, g-C_3N_4/$CdTiO_3$ nanocomposites were synthesized via sonication-assisted and in-situ hydrothermal routes. The influence of synthesis methodology on structural, optical, surface, and photocatalytic properties was systematically investigated using Rhodamine B as a model pollutant. The enhanced photocatalytic performance is discussed in terms of heterostructure formation, interfacial charge separation, and synergistic effects, providing valuable insights for the rational design of g-C_3N_4-based perovskite photocatalysts for wastewater treatment and environmental remediation.

2. Synthesis and Characterization

2.1. Materials

Melamine (Aldrich, 99.0%), $Cd(NO_3)_2$ (CDH, 98% metal-based), titanium isopropoxide (Aldrich, 99.0%), NaOH (CDH, 98.0%), and Rhodamine B (Aldrich, 85.0%) were used as received. All other chemicals employed in this study were of analytical grade and used without further purification.

2.2. Synthesis of $CdTiO_3$ Nanoparticles

$CdTiO_3$ nanoparticles were synthesized via a hydrothermal method from reported literature [22]. In a typical procedure, 3.43 mmol of $Cd(NO_3)_2$ was dissolved in 20 mL of double-distilled water, followed by the addition of 3.43 mmol of titanium isopropoxide. The resulting solution was stirred for 30 min to ensure complete mixing. Subsequently, 0.6 M NaOH (40 mL) was added dropwise, and the mixture was stirred for an additional 3 h. The resulting milky-white suspension was transferred into a Teflon-lined stainless-steel autoclave and heated at 180 °C for 16 h. After cooling to room temperature, the precipitate was collected, thoroughly washed with distilled water and ethanol, and dried for further characterization.

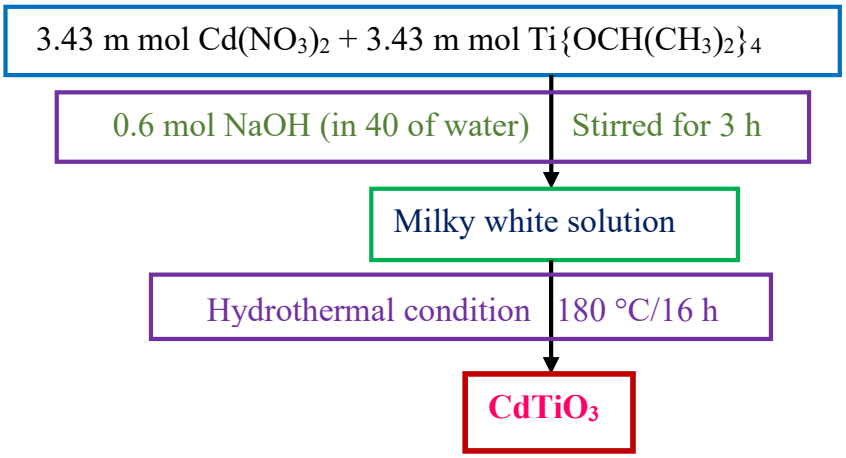

Scheme 1: Synthesis of $CdTiO_3$

2.3. Synthesis of Graphitic Carbon Nitride (g-C_3N_4)

Graphitic carbon nitride (g-C_3N_4) was synthesized via the thermal polymerization of melamine from reported literature [23,24]. In this process, melamine was placed in a covered alumina crucible and heated at 550 °C for 2 h under a nitrogen atmosphere. After cooling naturally to room temperature, a pale-yellow g-C_3N_4 powder was obtained. The as-prepared g-C_3N_4 was directly used for the subsequent nanocomposite synthesis.

2.4. Synthesis of g-C_3N_4–$CdTiO_3$ Nanocomposites

g-C_3N_4–$CdTiO_3$ nanocomposites were prepared using two different hydrothermal routes.

Sonication Route (Scheme 2): In this method, 80 mg of g-C_3N_4 was dispersed in 100 mL of deionized water and sonicated for 12 h to achieve uniform exfoliation. Subsequently, 715 mg of the as-synthesized $CdTiO_3$ nanoparticles was added to the dispersion. The resulting mixture was stirred and heated at 100 °C to evaporate the solvent, yielding a light-yellow g-C_3N_4–$CdTiO_3$ composite powder.

2.5. In-Situ Hydrothermal Route (Scheme 3): In this approach, 3.43 mmol of $Cd(NO_3)_2$ was dissolved in 20 mL of double-distilled water, followed by the addition of 3.43 mmol of titanium isopropoxide. The solution was stirred for 30 min, after which 0.6 mol NaOH dissolved in 40 mL of water was added, and stirring continued for 3 h to form a milky-white suspension. Then, 80 mg of g-C_3N_4 was introduced into the mixture and stirred for an additional 1 h. The resulting suspension was transferred into a Teflon-lined stainless-steel autoclave and heated at 180 °C for 16 h. After cooling to room temperature, the light-yellow g-C_3N_4–$CdTiO_3$ nanocomposite was collected, washed, and dried for further characterization.

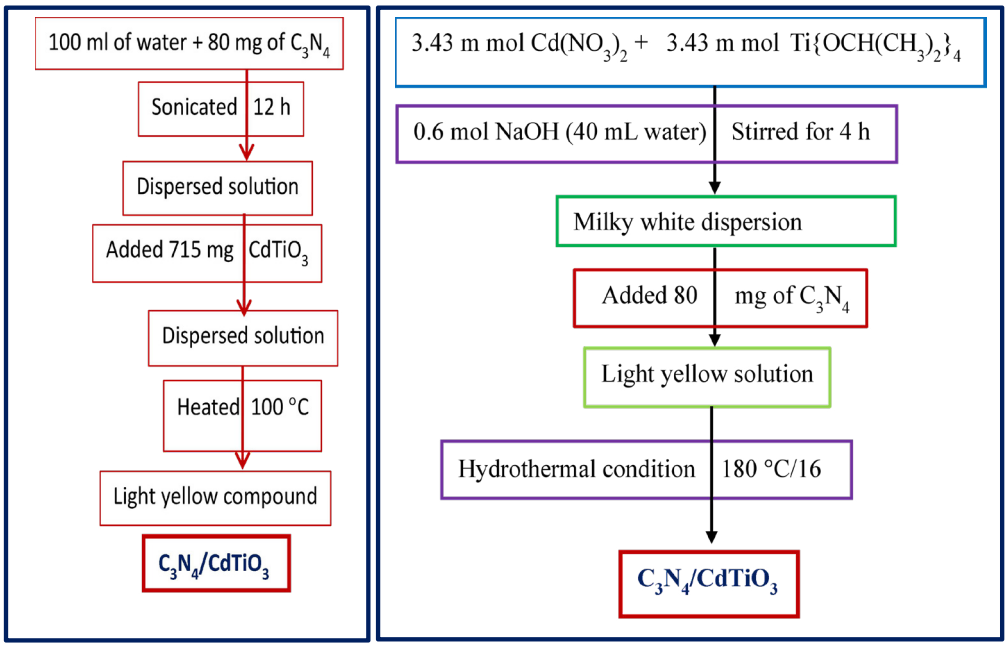

Scheme 2 and 3: Synthesis of g-C_3N_4–$CdTiO_3$ Nanocomposites by Sonication and in-Situ Route Respectively

2.6. Characterization

Powder X-ray diffraction studies (PXRD) were carried out using Ni filtered Cu-Kα radiation. Normal scans were recorded with a step size of 0.02° and step time of 1 s. The $K_{\alpha 2}$ reflections were removed to obtain accurate lattice constants. Field emission scanning electron microscopy (FESEM) was carried out by FEI quanta 3D FEG – FESEM operated at 10 kV. The pellet had been coated with gold. Transmission Electron Microscopy (TEM) studies were carried out using a Tecnai G^2 20 electron microscope operated at 200 KV. TEM specimens were prepared by dispersing the sample in ethanol by ultrasonic treatment, dropping onto a porous carbon film supported on a copper grid, and then drying in air. Nitrogen adsorption–desorption isotherms were recorded at liquid nitrogen temperature (77 K) using a Nova 2000e (Quantachrome Corp.) equipment and the specific area was determined by the Brunauer–Emmett–Teller (BET) method. The powder sample was degassed at 150 ºC for 6 h prior to the surface area measurements. Diffuse-reflectance spectra (DR) spectra were recorded on Shimadzu UV-2450 spectrophotometer where the baseline was fixed using a barium sulfate reference.

2.7. Photocatalytic Activity

Rhodamine B (RhB) was selected as a model dye to evaluate the visible-light-driven photocatalytic performance of the samples. Photocatalytic experiments were performed under visible-light irradiation using a 300 W Xe lamp solar simulator (Asahi Spectra Co., Ltd.). In a typical experiment, 25 mg of photocatalyst was dispersed in 100 mL of RhB aqueous solution (5 mg L^{-1}) and stirred at 250 rpm at room temperature. Prior to illumination, the suspension was stirred in the dark for 30 min to establish adsorption–desorption equilibrium. During photocatalysis, aliquots of the suspension were withdrawn at regular intervals, centrifuged to remove the photocatalyst, and analyzed for RhB concentration using a UV–Vis spectrophotometer. The degradation efficiency was calculated from the change in absorbance of the RhB solution over time.

3. Results and Discussion

3.1. PXRD Analysis and Phase Comparison

In this study, we determine the effect of heterostructure and synthesis process effect on the photocatalytic degradation of dye molecules using ambient stable g-C_3N_4–$CdTiO_3$ nanocomposites. Figure 1 and 2 shows the powder X-ray diffraction patterns of pure $CdTiO_3$ and g-C_3N_4. The PXRD pattern of the synthesized $CdTiO_3$ confirms the formation of a single-phase crystalline material. All the observed diffraction peaks can be well indexed to $CdTiO_3$ with a trigonal (hexagonal setting) structure, belonging to the space group R-3 (No. 148). No additional peaks corresponding to impurity phases such as CdO or TiO_2 are detected, indicating the high phase purity of the synthesized sample.

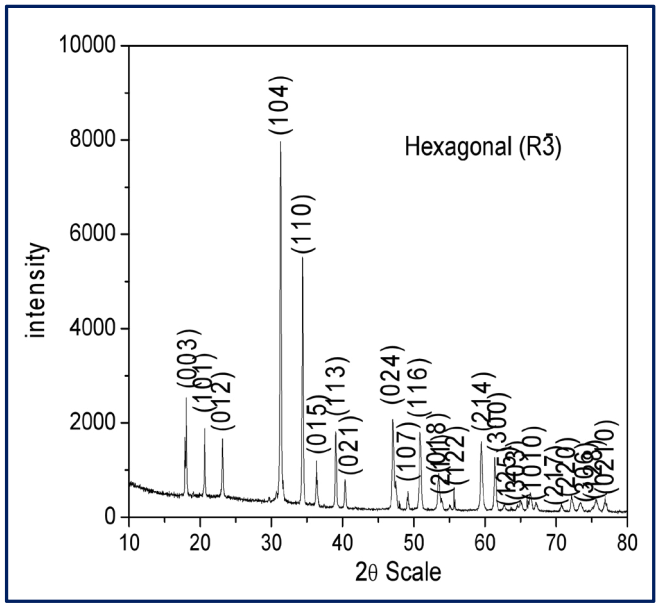

Figure 1: PXRD Patterns of Pure $CdTiO_3$

The sharp and intense diffraction peaks indicate good crystallinity of $CdTiO_3$. The stabilization of the R-3 symmetry suggests a distorted perovskite-type structure, where tilting and distortion of TiO_6 octahedra occur due to ionic size mismatch and lattice strain. Such structural distortion is commonly observed in Cd-based titanates and is consistent with previously reported PXRD studies. Based on PXRD analysis and comparison with standard crystallographic data, the lattice parameters of $CdTiO_3$ in the hexagonal (trigonal) R-3 structure are 5.4432 Å and c ≈ 13.1513 Å. These lattice parameters are in good agreement with reported values for trigonal $CdTiO_3$, confirming the successful formation of the desired crystal structure [25]. The PXRD pattern of the synthesized g-C_3N_4 exhibits two characteristic diffraction peaks, confirming the successful formation of graphitic carbon nitride.

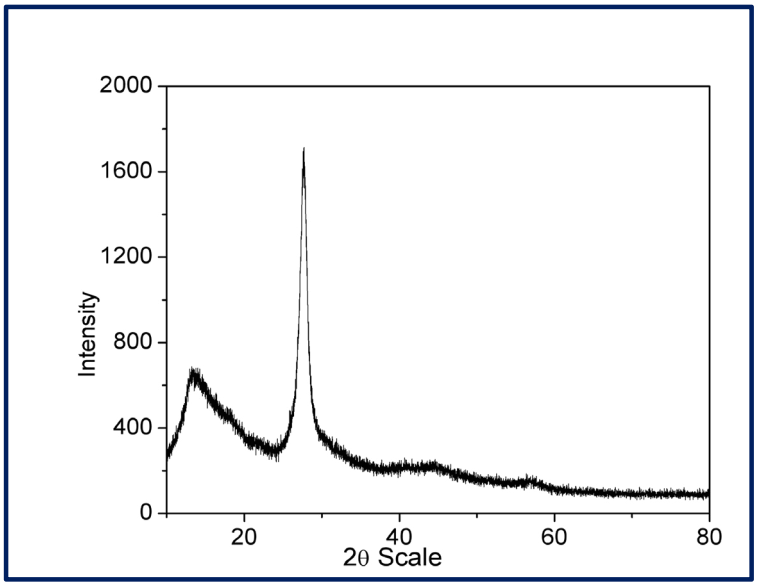

Figure 2: PXRD Patterns of Pure g-C_3N_4

The strong diffraction peak observed at 2θ ≈ 27.4° corresponds to the (002) plane, which arises from the interlayer stacking of conjugated aromatic systems within the graphitic structure. This peak reflects the periodic stacking of tri-s-triazine (heptazine) units along the c-axis. A weaker diffraction peak appearing at 2θ ≈ 13.0° is indexed to the (100) plane, which is associated with the in-plane structural packing of tri-s-triazine units within the g-C_3N_4 layers. The presence of these two characteristic peaks indicates

the formation of a layered, graphitic structure with moderate crystallinity. The relatively broad nature of the diffraction peaks suggests the poorly crystalline and polymeric nature of g-C_3N_4, which is typical for thermally polymerized carbon nitride. No impurity-related peaks are detected, confirming the high phase purity of the prepared g-C_3N_4. Graphitic carbon nitride crystallizes in a hexagonal structure, generally assigned to the space group $P6_3cm$ or closely related hexagonal symmetry. Based on standard PXRD analysis, the lattice parameters of g-C_3N_4 are approximately $a \approx 4.784$ and $c \approx 6.792$ Å. The interlayer distance (d_{002}) calculated from the (002) peak at ~27.4° is ~0.326 nm, which is consistent with reported values for graphitic carbon nitride [26].

The PXRD patterns of the g-C_3N_4/$CdTiO_3$ nanocomposites synthesized via sonication and in-situ routes are presented in the figure 3.

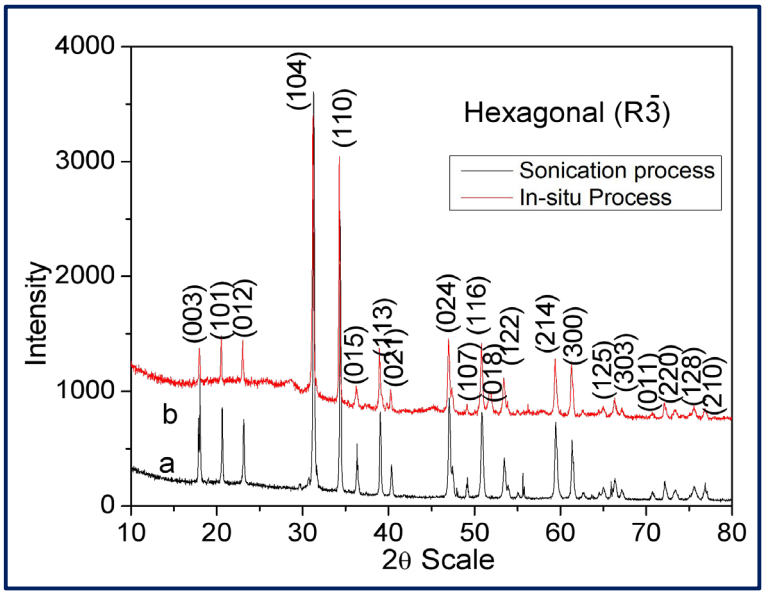

Figure 3: PXRD Patterns of g-C_3N_4/$CdTiO_3$ Nanocomposites

In both cases, the diffraction peaks corresponding to crystalline $CdTiO_3$ are clearly observed, confirming that the $CdTiO_3$ phase is well preserved after composite formation. The characteristic diffraction peak of g-C_3N_4 at $2\theta \approx 27.4°$, assigned to the (002) plane associated with interlayer stacking of graphitic sheets, is either weak or partially overlapped by the intense $CdTiO_3$ reflections. This behaviour is commonly reported for $CdTiO_3$–g-C_3N_4 composites and is attributed to the low content and poor crystallinity of g-C_3N_4 as well as its homogeneous dispersion on the $CdTiO_3$ surface. A comparison between the two synthesis routes reveals that the in-situ synthesized composite exhibits sharper and more intense diffraction peaks compared to the sonication-derived sample, indicating improved crystallinity and stronger interfacial interaction between $CdTiO_3$ and g-C_3N_4. In contrast, the sonication route shows slightly broadened peaks, suggesting smaller crystallite size and increased lattice strain due to physical mixing. Importantly, no additional impurity peaks corresponding to CdO, TiO_2, or other secondary phases are detected in either composite, confirming the phase purity and structural stability of $CdTiO_3$ during composite formation. Overall, the PXRD results confirm the successful formation of g-C_3N_4/$CdTiO_3$ nanocomposites, where $CdTiO_3$ retains its crystal structure while g-C_3N_4 is well integrated without altering the host lattice.

3.2. Morphological and Interfacial Analysis

The FESEM micrograph of $CdTiO_3$ (Figure 4) reveals an irregular, polycrystalline morphology composed of plate-like and block-shaped particles with non-uniform sizes consistent with reported hydrothermal $CdTiO_3$ morphologies [20]. The particles exhibit angular edges and faceted surfaces, indicating their crystalline nature. Lateral dimensions range from sub-micrometer to a few micrometers, as shown by the 5 µm scale bar. The particles are closely packed and moderately agglomerated, a common feature in oxide ceramics synthesized via wet-chemical or thermal methods, likely due to high surface energy and strong interparticle interactions during crystallization. The rough surface texture and fractured grain boundaries suggest that the microcrystals are aggregates of smaller primary crystallites. No spherical or fibrous structures were observed, confirming that $CdTiO_3$ predominantly forms irregular microcrystals rather than isotropic nanoparticles. The absence of secondary morphological features further supports the phase purity of the material, consistent with PXRD results. Overall, the FESEM analysis confirms the successful formation of crystalline $CdTiO_3$ with a dense, irregular microstructure, providing abundant surface sites favourable for interfacial contact in composite formation and catalytic applications.

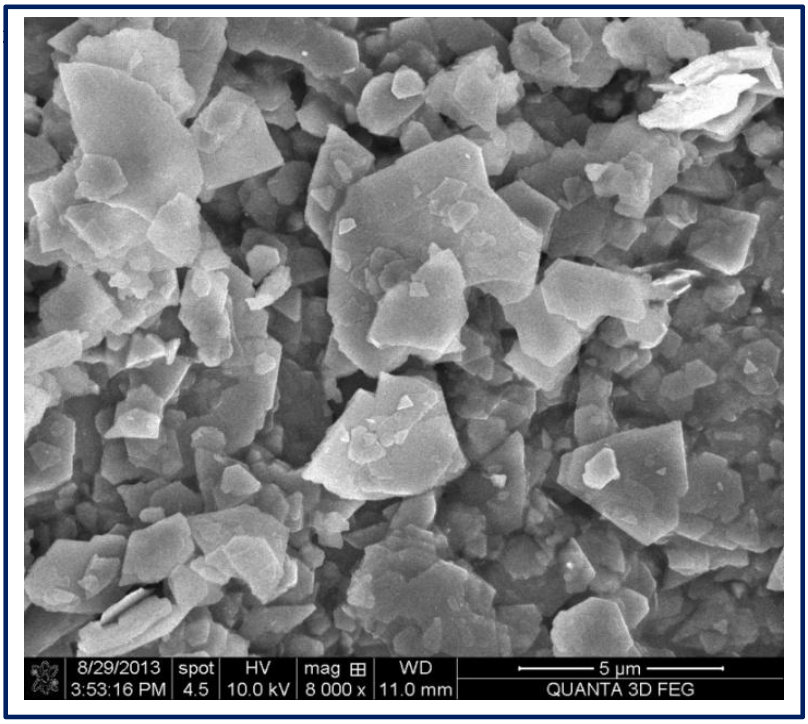

Figure 4: FESEM Micrograph of $CdTiO_3$

The figure 5 and 6 shows the TEM micrograph of g-C_3N_4/ $CdTiO_3$ nanocomposites synthesized by sonication and in-situ methodology respectively. The low-magnification TEM images reveal large, thin sheet-like structures with lateral dimensions extending up to several hundred nanometers (≈0.5–1 µm). The high electron transparency of the sheets confirms their ultrathin, few-layer nature, distinguishing them from bulk or thick plate-like particles. The presence of partially overlapped and restacked sheets is characteristic of exfoliated two-dimensional materials formed during sample drying.

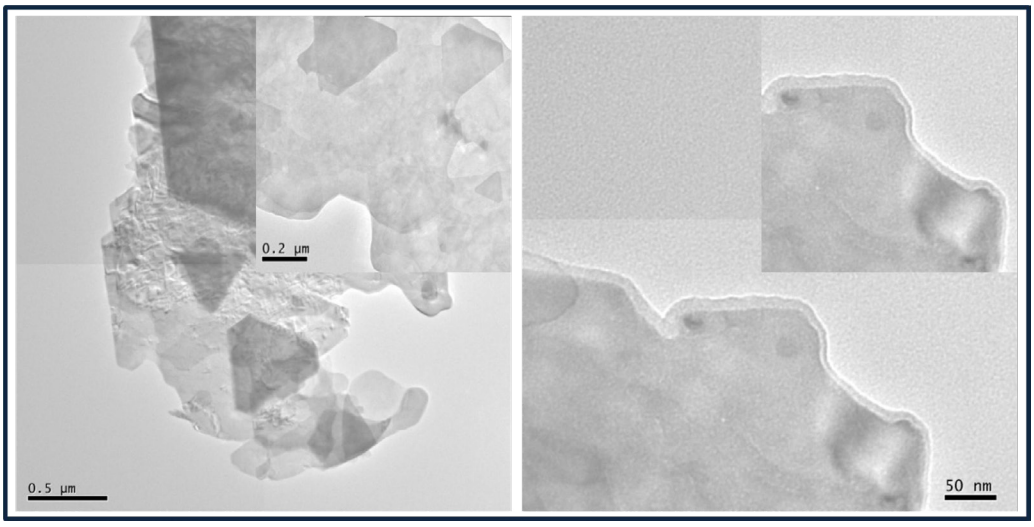

Figure 5: TEM Micrograph of g-C_3N_4/$CdTiO_3$ Nanocomposites Obtained by Sonication

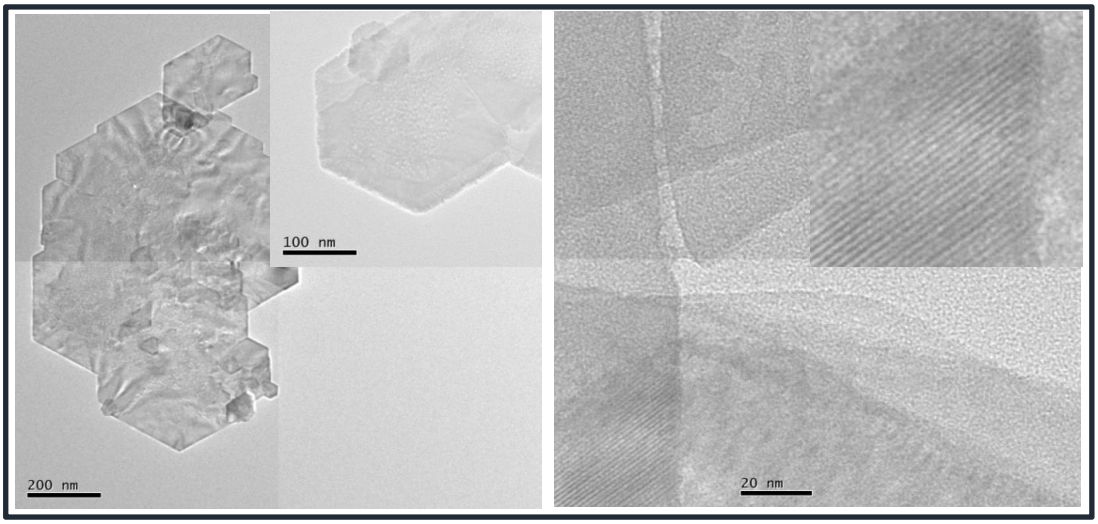

Figure 6: TEM Micrograph of g-C_3N_4/$CdTiO_3$ Nanocomposites Obtained by In-situ

The intermediate-magnification inset (scale bar 0.2 µm) shows irregular polygonal nanosheets with smooth and well-defined contours, indicating that the sheets retain good structural integrity after synthesis and processing. The absence of discrete nanoparticles or large agglomerates suggests a uniform nanosheet morphology rather than particulate growth.

High-magnification TEM images (scale bar 50 nm) further confirm the few-layer structure, showing clear sheet edges with slight thickness contrast. The contrast variation near the edges arises from edge folding and local thickness fluctuations, which are commonly observed in ultrathin g-C_3N_4 and oxide-based nanosheets. No phase-segregated regions or large crystalline grains are detected, implying homogeneous dispersion and intimate interfacial contact within the nanosheet framework. The high-resolution TEM (HRTEM) image exhibits distinct lattice fringes, confirming the presence of crystalline $CdTiO_3$ domains embedded within the nanosheet matrix. The surrounding low-contrast regions correspond to the amorphous or semicrystalline g-C_3N_4 phase. The close interfacial contact between the lattice-resolved $CdTiO_3$ domains and the g-C_3N_4 nanosheets provides direct structural evidence for the formation of a well-coupled heterojunction, which is favourable for efficient charge transfer. TEM analysis of the composites confirms ultrathin g-C_3N_4 nanosheets decorated with $CdTiO_3$ nanodomains. The in-situ composite exhibits more uniform dispersion and intimate interfacial contact than the sonication-derived sample, similar to trends reported for in-situ-grown g-C_3N_4 heterostructures [27,28].

3.3. Surface Area Analysis

The BET surface area of pristine $CdTiO_3$ (95 $m^2\ g^{-1}$) is higher than that of bulk g-C_3N_4 (56 $m^2\ g^{-1}$), reflecting the comparatively finer oxide particles and better intrinsic porosity of $CdTiO_3$ and consistent with reported values [21,29]. Upon forming the g-C_3N_4/$CdTiO_3$ heterostructure, a pronounced increase in surface area is observed, confirming effective interfacial engineering between the two components.

The sonication-assisted composite exhibits a surface area of 143 $m^2\ g^{-1}$, which is significantly higher than those of the individual constituents. This enhancement originates from ultrasonic exfoliation of g-C_3N_4 layers and the uniform anchoring of $CdTiO_3$ nanoparticles onto the g-C_3N_4 sheets, which suppresses restacking and creates additional exposed active sites. Notably, the in-situ synthesized g-C_3N_4/$CdTiO_3$ composite shows the highest surface area (187 $m^2\ g^{-1}$). This superior value is attributed to the simultaneous nucleation and growth of $CdTiO_3$ directly on the g-C_3N_4 framework, leading to a highly dispersed heterointerface, hierarchical porosity, and strong interfacial contact. The in-situ route effectively prevents particle agglomeration and maximizes pore accessibility.

Overall, the progressively increased surface area from pristine materials to sonication-assisted and finally in-situ composites demonstrates that in-situ heterostructure formation is the most effective strategy for generating a high-surface-area photocatalyst, which is expected to enhance adsorption capacity, charge separation efficiency, and catalytic performance. Comparable increases have been reported in g-C_3N_4-based heterostructures and are directly correlated with enhanced photocatalytic performance [30-32].

3.4. Diffuse Reflectance Spectra Analysis

The pristine g-C_3N_4 sample exhibits an absorption edge at approximately 450 nm, corresponding to a band gap energy of 2.76 eV, confirming its effective photoactivation under visible-light irradiation. In contrast, $CdTiO_3$ displays a wider band gap of 3.67 eV, indicating that it is primarily UV-active with limited visible-light absorption agree well with literature reports [6,20]. The wide band gap of $CdTiO_3$ complements the visible-light-responsive g-C_3N_4, facilitating the formation of a heterojunction that enhances charge separation and suppresses electron–hole recombination. Upon heterostructure formation, the band gaps of

the g-C_3N_4/$CdTiO_3$ composites were determined to be 2.92 eV and 2.95 eV for the sonication and in-situ synthesis routes, respectively. These values confirm that the heterostructured photocatalysts retain visible-light activity, while the slight band-gap widening can be attributed to interfacial interactions and electronic structure modulation between g-C_3N_4 and $CdTiO_3$.

In the g-C_3N_4/$CdTiO_3$ heterostructure, the charge-transfer behaviour is best described by an S-scheme heterojunction. g-C_3N_4, with a narrower band gap (~2.76 eV), is efficiently excited under visible-light irradiation, whereas $CdTiO_3$, possessing a wider band gap (~3.67 eV), is primarily UV-active and mainly functions as a charge-separation promoter under visible light. Upon intimate interfacial contact, Fermi-level equilibration between g-C_3N_4 and $CdTiO_3$ induces band bending and establishes an internal electric field at the heterointerface.

Under light excitation, the interfacial electric field drives the recombination of photogenerated electrons in the conduction band of $CdTiO_3$ with holes in the valence band of g-C_3N_4, selectively removing charge carriers with weak redox ability. Consequently, highly reductive electrons remain in the conduction band of g-C_3N_4, while strongly oxidative holes accumulate in the valence band of $CdTiO_3$. This S-scheme charge-transfer pathway effectively suppresses electron–hole recombination while preserving strong redox potentials, thereby accounting for the enhanced photocatalytic performance of the g-C_3N_4/$CdTiO_3$ composite under visible-light irradiation. Slight band-gap widening in the composites has also been observed in similar heterostructures and is attributed to interfacial electronic interactions rather than quantum confinement effects [33].

3.5. Photocatalytic Performance Analysis

The photocatalytic degradation efficiency of the samples was evaluated by monitoring the normalized concentration ratio (C/C_0) as a function of irradiation time, as shown in the figure 7. $CdTiO_3$ exhibits the lowest photocatalytic activity, with only a marginal decrease in C/C_0 even after prolonged irradiation, which can be attributed to its wide band gap and limited visible-light absorption, resulting in inefficient photoexcitation and rapid charge recombination. In contrast, g-C_3N_4 shows improved photocatalytic performance compared to $CdTiO_3$, owing to its visible-light responsiveness. However, the degradation rate remains moderate, likely due to fast recombination of photogenerated charge carriers in the absence of an efficient charge-separation pathway.

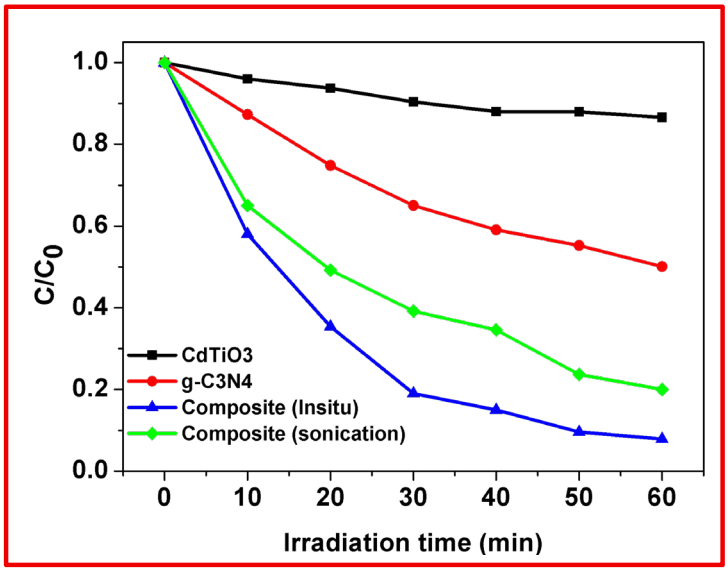

Figure 7: Comparison of Photocatalytic Activities of Pure $CdTiO_3$, g-C_3N_4, g-C_3N_4/$CdTiO_3$ (In-situ and Sonication) for the Degradation of RhB Under Visible Light

Both g-C_3N_4/$CdTiO_3$ nanocomposites demonstrate significantly enhanced photocatalytic activity, confirming the beneficial role of heterojunction formation. Among them, the in-situ synthesized composite exhibits the highest degradation efficiency, achieving a rapid and continuous decrease in C/C_0 with irradiation time. The superior performance of the in-situ composite is attributed to stronger interfacial coupling, more intimate contact between g-C_3N_4 and $CdTiO_3$ nanosheets, and more efficient charge separation, which suppresses electron–hole recombination. The sonication-derived composite also shows enhanced activity compared to the pristine components but is slightly less effective than the in-situ sample, likely due to comparatively weaker interfacial interaction and less uniform heterojunction formation. The in-situ g-C_3N_4/$CdTiO_3$ composite exhibits superior RhB degradation efficiency compared to pristine g-C_3N_4 and $CdTiO_3$, consistent with reports on perovskite/g-C_3N_4 systems [34-36]. The enhanced performance is attributed to improved charge separation, higher surface area, and strong interfacial coupling.

3.6. Stability and Repeatability of the Photocatalyst

The reusability and stability of the g-C_3N_4/$CdTiO_3$ photocatalyst were evaluated through consecutive photocatalytic degradation cycles, as illustrated in the figure 8. The degradation efficiency remains high and only slightly decreases over successive runs, indicating that the catalyst retains most of its photocatalytic activity even after repeated use. The marginal reduction in performance observed after multiple cycles can be attributed to minor loss of active surface sites, partial adsorption of reaction intermediates, or slight catalyst loss during recovery and washing steps, rather than structural degradation.

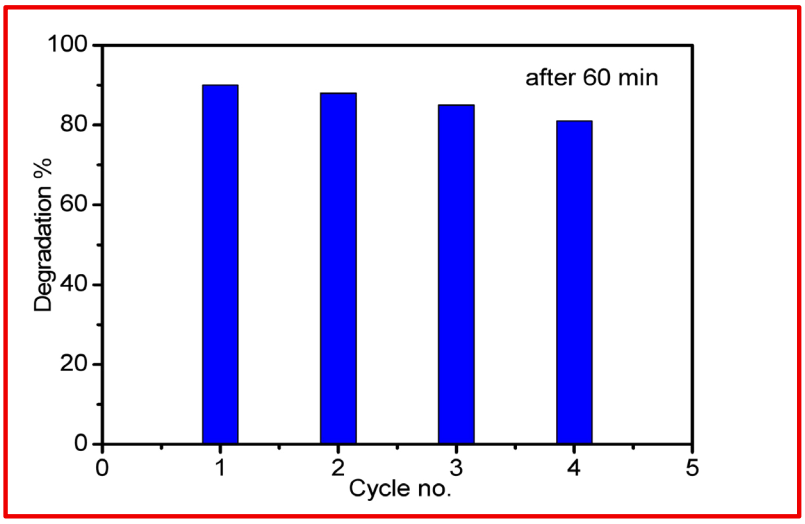

Figure 8: Recyclability of the g-C_3N_4/$CdTiO_3$ (In-situ) Photocatalyst for the Degradation of RhB Under Visible Light Irradiation (Five Successive Experimental Runs)

Importantly, no abrupt decline in activity is observed, confirming the good structural stability and repeatability of the composite photocatalyst under the applied reaction conditions. The consistent performance across cycles demonstrates that the g-C_3N_4/$CdTiO_3$ heterostructure is robust, with strong interfacial interaction between g-C_3N_4 and $CdTiO_3$ effectively preventing photocorrosion and maintaining efficient charge transfer during repeated photocatalytic reactions. The composite shows excellent stability over repeated cycles better than similar g-C_3N_4-based photocatalysts reported in literature [37,38]. The absence of significant activity loss confirms structural robustness and resistance to photocorrosion.

3.7. Proposed Photocatalytic Mechanism of g-C_3N_4/$CdTiO_3$ Heterostructure

Under light irradiation, both g-C_3N_4 and $CdTiO_3$ are photoexcited, generating electron–hole pairs in their respective conduction and valence bands. Due to the intimate interfacial contact formed between the g-C_3N_4 nanosheets and $CdTiO_3$ nanosheets, a built-in electric field develops at the heterointerface, which drives directional charge migration. Based on the relative band edge positions, photogenerated electrons in the conduction band (CB) of g-C_3N_4 transfer to the CB of $CdTiO_3$, while holes in the valence band (VB) of $CdTiO_3$ migrate toward the VB of g-C_3N_4, forming an effective S-scheme heterojunction (figure 9). The photocatalytic process proceeds via an, preserving strong redox potentials while suppressing recombination. This mechanism has been widely accepted for g-C_3N_4-based heterostructures and explains the enhanced activity observed in this study [39-41]. This spatial separation of electrons and holes significantly suppresses their recombination and prolongs charge carrier lifetimes. The accumulated electrons on the $CdTiO_3$ surface react with dissolved oxygen to generate reactive oxygen species such as $\bullet O_2^-$ radicals, while the holes retained on g-C_3N_4 oxidize surface-adsorbed water molecules or organic pollutants to produce •OH radicals. These highly reactive species are primarily responsible for the degradation of organic contaminants during the photocatalytic process. Furthermore, the nanosheet-based architecture provides a large interfacial area and short charge diffusion paths, ensuring efficient charge transport and utilization. The heterostructure also stabilizes the individual components by reducing charge accumulation and photocorrosion, leading to excellent recyclability and long-term photocatalytic stability.

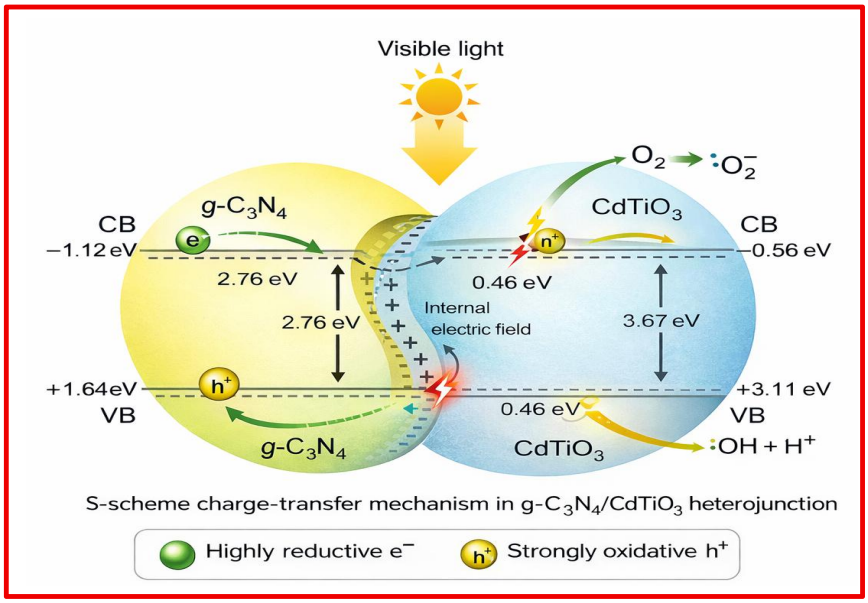

Figure 9: Schematic Diagram of the Mechanism for High Separation Efficiency of Photoinduced Charge Carrier and Transfer in the $g\text{-}C_3N_4/CdTiO_3$ System Under Visible Light Irradiation

4. Conclusion

In summary, g-C_3N_4/$CdTiO_3$ nanocomposites were successfully synthesized via sonication-assisted and in-situ hydrothermal routes, and their structural, morphological, optical, surface, and photocatalytic properties were systematically investigated. PXRD and microscopic analyses confirmed the formation of crystalline $CdTiO_3$ and the successful construction of intimate g-C_3N_4–$CdTiO_3$ heterostructures, with the synthesis route playing a crucial role in determining interfacial contact and microstructural features. The in-situ hydrothermal method produced a more homogeneous dispersion of $CdTiO_3$ on g-C_3N_4, resulting in enhanced interfacial interaction compared to the sonication route.

The g-C_3N_4/$CdTiO_3$ nanocomposites exhibited significantly enhanced visible-light-driven photocatalytic degradation of Rhodamine B relative to pristine g-C_3N_4 and $CdTiO_3$. This improvement is attributed to extended visible-light absorption, increased surface-active sites, and effective suppression of electron–hole recombination due to heterostructure formation. The photocatalytic process is governed by an S-scheme charge-transfer mechanism, which preserves the strong redox capability of photogenerated charge carriers and promotes efficient dye degradation.

Furthermore, the nanocomposite demonstrated good structural stability and repeatable photocatalytic performance over multiple degradation cycles, indicating its robustness and reusability. This study highlights the potential of $CdTiO_3$ as an effective perovskite partner for g-C_3N_4 and provides new insight into the design of g-C_3N_4-based heterostructured photocatalysts. The findings offer a promising strategy for developing efficient visible-light-responsive photocatalysts for dye-contaminated wastewater treatment.

Acknowledgments

PKP and BK thanks ANRF for providing support through the grant no SUR/2022/004717. The authors also thank IIT Delhi and IISER Berhampur India for some of reaction and characterization facility.

Author Contributions

Pramendra Kumar Pandey and Revati Raman Chaubey: Synthesis and draft writing, Gyandeshwar Kumar Rao and Arvind Kumar Singh: Characterization, Bharat Kumar: Concept, synthesis modification, final draft writing and final submission. All the authors reviewed the manuscript.

Funding

Funding is not applicable

Declarations

Clinical Trial

Clinical trial is not applicable in the manuscript.

Consent to Publish Declaration

Not applicable

Ethics and Consent to Participate Declarations

Not applicable

Competing Interests

The authors declare no competing interests

Data Availability

The authors declare that the data supporting the findings of this study are available within the paper file. Should any raw data files be needed in another format they are available from the

corresponding author upon reasonable request.

References

1. Fujishima, A., & Honda, K. (1972). Electrochemical photolysis of water at a semiconductor electrode. *nature, 238*(5358), 37-38.
2. Hoffmann, M. R., Martin, S. T., Choi, W., & Bahnemann, D. W. (1995). Environmental applications of semiconductor photocatalysis. *Chemical reviews, 95*(1), 69-96.
3. Chen, X., Shen, S., Guo, L., & Mao, S. S. (2010). Semiconductor-based photocatalytic hydrogen generation. *Chemical reviews, 110*(11), 6503-6570.
4. Linsebigler, A. L., Lu, G., & Yates Jr, J. T. (1995). Photocatalysis on TiO_2 surfaces: principles, mechanisms, and selected results. Chemical reviews, 95(3), 735-758.
5. Janotti, A., & Van de Walle, C. G. (2009). Fundamentals of zinc oxide as a semiconductor. *Reports on progress in physics, 72*(12), 126501.
6. Wang, X., Maeda, K., Thomas, A., Takanabe, K., Xin, G., Carlsson, J. M., ... & Antonietti, M. (2009). A metal-free polymeric photocatalyst for hydrogen production from water under visible light. *Nature materials, 8*(1), 76-80.
7. Thomas, A., Fischer, A., Goettmann, F., Antonietti, M., Müller, J. O., Schlögl, R., & Carlsson, J. M. (2008). Graphitic carbon nitride materials: variation of structure and morphology and their use as metal-free catalysts. *Journal of Materials Chemistry, 18*(41), 4893-4908.
8. Ong, W. J., Tan, L. L., Ng, Y. H., Yong, S. T., & Chai, S. P. (2016). Graphitic carbon nitride (g-C3N4)-based photocatalysts for artificial photosynthesis and environmental remediation: are we a step closer to achieving sustainability?. *Chemical reviews, 116*(12), 7159-7329.
9. Zhang, J., Chen, Y., & Wang, X. (2015). Two-dimensional covalent carbon nitride nanosheets: synthesis, functionalization, and applications. *Energy & Environmental Science, 8*(11), 3092-3108.
10. Wang, Y., Wang, X., & Antonietti, M. (2012). Polymeric graphitic carbon nitride as a heterogeneous organocatalyst: from photochemistry to multipurpose catalysis to sustainable chemistry. *Angewandte Chemie International Edition, 51*(1), 68-89.
11. Cao, S., Low, J., Yu, J., & Jaroniec, M. (2015). Polymeric photocatalysts based on graphitic carbon nitride. *Advanced Materials, 27*(13), 2150-2176.
12. Zhang, G., Zhang, J., Zhang, M., & Wang, X. (2012). Polycondensation of thiourea into carbon nitride semiconductors as visible light photocatalysts. *Journal of Materials Chemistry, 22*(16), 8083-8091.
13. Dong, F., Wang, Z., Sun, Y., Ho, W. K., & Zhang, H. (2013). Engineering the nanoarchitecture and texture of polymeric carbon nitride semiconductor for enhanced visible light photocatalytic activity. *Journal of colloid and interface science, 401*, 70-79.
14. Liu, J., Liu, Y., Liu, N., Han, Y., Zhang, X., Huang, H., ... & Kang, Z. (2015). Metal-free efficient photocatalyst for stable visible water splitting via a two-electron pathway. *Science, 347*(6225), 970-974.
15. Dong, G., Zhao, K., & Zhang, L. (2012). Carbon self-doping induced high electronic conductivity and photoreactivity of gC_3N_4. *Chemical Communications, 48*(49), 6178-6180.
16. Guo, Y., Shoyama, K., Sato, W., Matsuo, Y., Inoue, K., Harano, K., ... & Nakamura, E. (2015). Chemical pathways connecting lead (II) iodide and perovskite via polymeric plumbate (II) fiber. *Journal of the American Chemical Society, 137*(50), 15907-15914.
17. Low, J., Yu, J., Jaroniec, M., Wageh, S., & Al-Ghamdi, A. A. (2017). Heterojunction photocatalysts. *Advanced materials, 29*(20), 1601694.
18. Li, X., Yu, J., Wageh, S., Al-Ghamdi, A. A., & Xie, J. (2016). Graphene in photocatalysis: a review. *small, 12*(48), 6640-6696.
19. Peña, M. A., & Fierro, J. L. G. (2001). Chemical structures and performance of perovskite oxides. *Chemical reviews, 101*(7), 1981-2018.
20. Yang, L. Y., Feng, G. P., Wang, T. X., Zhang, J. M., Lou,T. J. (2011) Low temperature preparation and characterization of $CdTiO_3$ nanoplates. *Materials Letters, 65*(17-18), 2601-2603.
21. Imran, Z., Rafiq, M. A., Hasan, M. M. (2014). Charge carrier transport mechanisms in perovskite $CdTiO_3$ fibers Open Access. *AIP Advances 4*, 067137.
22. Pandey, P. K., Chaubey, R. R., Rao, G. K., Srivastava, S., Singh, A. K., Kumar, B. (2026). Facile and Eco-friendly One Step Low Temperature Synthesis of Very Large Scale ATiO3 (A = Ca, Sr, Ba and Cd). *J App Mat Sci & Engg Res, 10*(1), 01-10.
23. Zhang, Y., Pan, Q., Chai, G. et al. (2013). Synthesis and luminescence mechanism of multicolor-emitting g-C_3N_4 nanopowders by low temperature thermal condensation of melamine. *Sci Rep 3,* 1943.
24. Wang, Z., Huang, Y., Ho, W., Cao, J., Shen, Z., & Lee, S. C. (2016). Fabrication of $Bi_2O_2CO_3$/g-C_3N_4 heterojunctions for efficiently photocatalytic NO in air removal: in-situ self-sacrificial synthesis, characterizations and mechanistic study. Applied Catalysis B: Environmental, 199, 123-133.
25. Yu, J., Wang, Y., & Xiao, W. (2013). Enhanced photoelectrocatalytic performance of SnO_2/TiO_2 rutile composite films. *Journal of Materials Chemistry A, 1*(36), 10727-10735.
26. Zhang, C., Liu, J., Huang, X., Chen, D., Xu, S. (2019). Multistage Polymerization Design for g-C_3N_4 Nanosheets with Enhanced Photocatalytic Activity by Modifying the Polymerization Process of Melamine. *ACS Omega, 4*(17), 17148-17159
27. Liu, G., Wang, L., Yang, H. G., Cheng, H. M., & Lu, G. Q. M. (2010). Titania-based photocatalysts—crystal growth, doping and heterostructuring. *Journal of Materials Chemistry, 20*(5), 831-843.
28. Wang, J., Tang, L., Zeng, G., Deng, Y., Dong, H., Liu, Y., ... & Chen, F. (2018). 0D/2D interface engineering of carbon quantum dots modified Bi_2WO_6 ultrathin nanosheets with enhanced photoactivity for full spectrum light utilization and mechanism insight. *Applied Catalysis B: Environmental, 222*,

115-123.
29. Alaghmandfard, A., Ghandi, K. (2022). A Comprehensive Review of Graphitic Carbon Nitride (g-C_3N_4)–Metal Oxide-Based Nanocomposites: Potential for Photocatalysis and Sensing. *Nanomaterials, 12*(2), 294.
30. Zhang, X., Yang, P. (2025). Tungsten Oxide/g-C_3N_4 Heterostructures: Composition, Structure, and Photocatalytic Applications. *Langmuir, 41*(11), 7191-7211
31. Zhang, Y., Mori, T., Ye, J., & Antonietti, M. (2010). Phosphorus-doped carbon nitride solid: enhanced electrical conductivity and photocurrent generation. *Journal of the American Chemical Society, 132*(18), 6294-6295.
32. Chen, X., Zhang, J., Fu, X., Antonietti, M., & Wang, X. (2009). Fe-g-C_3N_4-catalyzed oxidation of benzene to phenol using hydrogen peroxide and visible light. *Journal of the American Chemical Society, 131*(33), 11658-11659.
33. Di, J., Xia, J., Ji, M., Wang, B., Yin, S., Zhang, Q., ... & Li, H. (2016). Advanced photocatalytic performance of graphene-like BN modified BiOBr flower-like materials for the removal of pollutants and mechanism insight. *Applied Catalysis B: Environmental, 183,* 254-262.
34. Yang, Z. M., Huang, G. F., Huang, W. Q., Wei, J. M., Yan, X. G., Liu, Y. Y., ... & Pan, A. (2014). Novel Ag_3PO_4/CeO_2 composite with high efficiency and stability for photocatalytic applications. *Journal of Materials Chemistry A, 2*(6), 1750-1756.
35. Muthuganesh, A., Jacob, I. D., Soundranayagam, J. P., Surender, S., Elangovan, P., & Flora, X. H. (2024). Fabrication of g-C3N4/CuS heterostructures for efficient visible light-driven photocatalysts. *Inorganic Chemistry Communications, 159*, 111813.
36. Tan, Q., Kong, Z., Chen, X., Zhang, L., Hu, X., Mu, M., ... & Xu, B. (2019). Synthesis of SnO_2/graphene composite anode materials for lithium-ion batteries. *Applied Surface Science, 485*, 314-322.
37. Dong, F., Wu, L., Sun, Y., Fu, M., Wu, Z., & Lee, S. C. (2011). Efficient synthesis of polymeric g-C_3N_4 layered materials as novel efficient visible light driven photocatalysts. *Journal of Materials Chemistry, 21*(39), 15171-15174.
38. Liao, G., Yao, W. (2022). Facile synthesis of porous isotype heterojunction g-C_3N_4 for enhanced photocatalytic degradation of RhB under visible light. *Diamond and Related Materials, 128*, 109227.
39. Fu, J., Xu, Q., Low, J., Jiang, C., & Yu, J. (2019). Ultrathin 2D/2D WO_3/g-C_3N_4 step-scheme H2-production photocatalyst. *Applied Catalysis B: Environmental, 243*, 556-565.
40. Zhou, P., Yu, J., & Jaroniec, M. (2014). All-solid-state Z-scheme photocatalytic systems. *Advanced Materials, 26*(29), 4920-4935.
41. Prusova, B., Licek, J., Kumsta, M., Baron, M., & Sochor, J. (2020). Polyphenolic composition of grape stems. *Notulae Botanicae Horti Agrobotanici Cluj-Napoca, 48*(3), 1543-1559.